Maneuverability of an SMA-Embedded Soft/Rigid (Hybrid) Flagellated Swimmer in a Viscous Environment

Elif Pinar Aydin[1], Yasemin Ozkan-Aydin[1,*]

***Abstract*— Locomotion at low Reynolds number requires non-reciprocal deformation to generate net propulsion. While many low Reynolds number robotic swimmers can achieve straight motion, swimmers that can switch between straight swimming and turning through controlled changes in flagellar morphology remain underexplored. We present a soft–rigid hybrid flagellated robotic swimmer that achieves embodied maneuverability by morphology-modulated propulsion through embedded shape memory alloy (SMA) actuation. The robot operates in glycerine under low-Re conditions and uses a planar beating flagellum. Experiments demonstrate stable forward locomotion with speeds up to 7.96 ± 0.10 mm/s. Upon SMA activation, the swimmer achieves sustained steering with yaw rates up to 3.62 ± 0.58°/s. Controlled morphological asymmetry, generated through compact and localized SMA actuation, enables stable maneuverability while maintaining a minimal system footprint, offering a scalable strategy for adaptive low-Re robotic swimming.**

Soft robotics, low Reynolds number swimming, flagellar propulsion, bio-inspired locomotion

I. Introduction

Micro-robots represent a rapidly expanding research area due to their potential applications in targeted drug delivery, environmental monitoring, and microsurgery [1] [2]. In these contexts, such systems operate in fluid environments dominated by viscous forces, where inertial effects are negligible, a regime characterized by low Reynolds number. Locomotion under these conditions is fundamentally constrained: time-reversible or symmetric motions cannot generate net displacement, as described by Purcell's scallop theorem [3]. As a result, breaking spatial or temporal symmetry becomes essential for propulsion. Moreover, at micro scales, limited actuation capabilities, such as the lack of onboard motors or multiple independent inputs, combined with the unique fluid dynamics, render conventional swimming strategies ineffective. To address these constraints, researchers turn to biological systems that naturally operate in low-Reynolds-number environments, translating principles from microorganism locomotion into artificial swimmer design.

Microorganisms generate propulsion in viscous environments through highly specialized appendages that produce non-reciprocal motion, thereby overcoming the constraints of low-Reynolds-number hydrodynamics. Bacteria, for example, achieve locomotion via the continuous rotation of rigid helical flagella [4]. Eukaryotic cells such as algae and spermatozoa rely on the coordinated elastohydrodynamic deformation of flexible filaments to produce traveling bending waves that drive propulsion [5]. Beyond forward propulsion, microorganisms achieve maneuverability by dynamically modulating their body and appendage kinematics, suggesting that time-varying morphological asymmetry can provide an effective steering mechanism at low Reynolds number [6] [7].

Drawing inspiration from these biological paradigms [8]–[11], roboticists have developed artificial swimmers tailored for low-Reynolds-number navigation. Despite significant advances, the maneuverability of existing platforms remains constrained by limited structural compliance, restricted ac-

[1]Department of Electrical Engineering, University of Notre Dame, Notre Dame IN 46556, USA
*Corresponding author:yozkanay@nd.edu

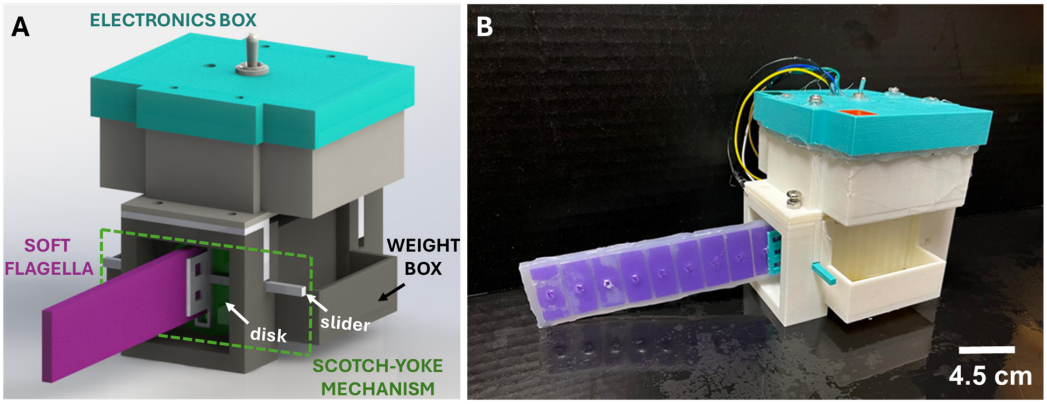


Fig. 1. **A soft/hybrid, single-flagellum macro robot designed for low Reynolds number locomotion.** (A) Schematic of the robot showing the Scotch-yoke mechanism driving the flagellum for oscillatory propulsion. The mechanism is enclosed in an electronics housing and stabilized by an added weight box. (B) Side view of the real robot.

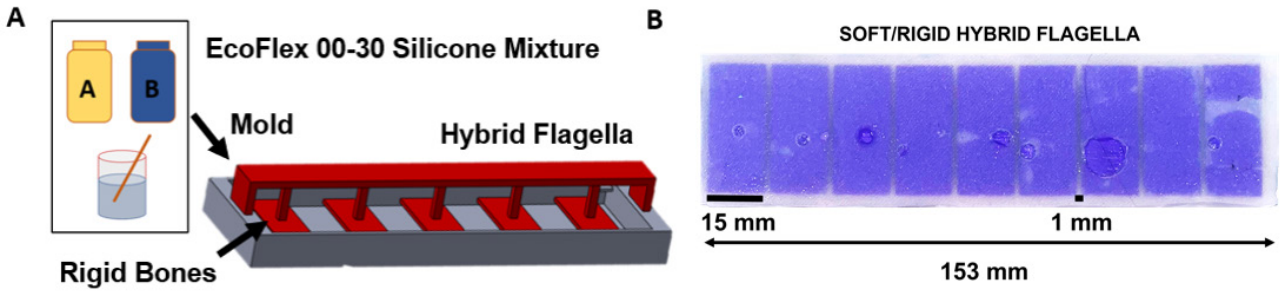


Fig. 2. **Fabrication of the soft/rigid (hybrid) flagella. (A)** Fabrication of the flagellum using a two-part Ecoflex 00-30 silicone, where mixed components A and B are cast to form the hybrid flagellum with PLA rigid bones. **(B)** The fabricated flagella with 3D printed PLA rigid bones (width=15 mm) embedded in a 153 mm flagella with 1 mm distance.

tuation capabilities, and insufficient morphological adaptability. Steering authority is particularly limited in single-flagellum systems..

While a compliant, high-degree-of-freedom flagellum provides a large deformation space for complex maneuvers, it also introduces substantial challenges in modeling and control. In such systems, locomotion cannot generally be represented by a simple static mapping between motor input and body kinematics. Instead, flagellar deformation emerges from the coupled interaction between structural elasticity and viscous fluid loading [12] [13]. This elastohydrodynamic coupling can produce strongly parameter-dependent deformation patterns and, in some cases, abrupt transitions in filament shape and propulsive force.

In this study, we experimentally investigate the maneuverability of an embodied soft–rigid hybrid single-flagellated swimmer operating in glycerine under low-Reynolds-number conditions (Fig. 1). Building on our previous characterization of planar-beating flagellar propulsion under symmetric actuation [14], we introduce morphology-based steering through an embedded shape memory alloy (SMA) actuator within the compliant flagellum. The flagellar structure preserves the flexibility required for wave-like deformation while providing sufficient support for stable axial alignment. Compact and embeddable SMA actuation locally modifies the flagellar curvature, introducing controllable morphological asymmetry without additional external linkages and enabling transitions between near-straight swimming and directional turning. Swimming performance is evaluated through measurements of forward velocity and turning characteristics, providing an experimental characterization of SMA-driven morphological steering in low-Reynolds-number locomotion.

II. Materials and Methods

A. Biological Inspiration

The undulatory locomotion of our soft/rigid (hybrid) flagella draws direct inspiration from the flagellar kinematics of eukaryotic microorganisms, such as spermatozoa and zoospores. In these biological systems, propulsion is achieved through the coordinated activity of an axoneme, a complex microtubule scaffold powered by thousands of dynein motor proteins distributed along its length [15]. This "active" actuation allows the organism to generate internal bending moments locally, resulting in highly controlled, planar or helical wave propagation.

In contrast, replicating such high-density, distributed actuation at the micro- or milli-scale presents immense fabrication challenges. Our approach simplifies this architecture by transitioning from active internal shearing to passive elastohydrodynamic coupling. By applying a periodic torque or displacement at the proximal end (the "head") of a flexible filament, we rely on the elasticity of our flagella and fluid's viscous resistance to deform the material in a wave-like fashion. The resulting spatiotemporal deformation, which is driven by the balance between the material's bending stiffness and the fluid's drag, breaks the time-reversal symmetry required for locomotion in low Reynolds number ($Re \ll 1$) regimes.

B. Mechanical and Electrical Design

a) Robot Body and Electronics: It is designed in SolidWorks and fabricated using a Bambu Lab X1C 3D printer (Fig.1). The structure consists of a base and an electronic compartment housing the control and power components, including an Arduino Pro Mini, a TB6612 motor driver, and MOSFET switching circuitry for the SMA actuator. The system is powered by a 7.4 V, 1000 mAh LiPo battery, which supplies both the DC motor and the control electronics, including the SMA actuation circuit.

Propulsion is generated by a 6V, 100 RPM DC gear motor that drives a Scotch–Yoke mechanism. The Scoth-Yoke converts continuous rotational motion into linear movement at the base of the flagellum (SI Movie 00:06-00:10). This linear excitation produces approximately sinusoidal oscillations, using the elastic compliance of the soft/rigid (hyrid) flagellum that enables smooth propagation of motion from base to tip (Fig. 1A).

A single light-dependent resistor (LDR) is incorporated into a voltage-divider circuit and connected to an analog input of the Arduino. When the measured light intensity exceeds a predefined threshold, a coupled control response is triggered: (i) the embedded shape memory alloy (SMA)

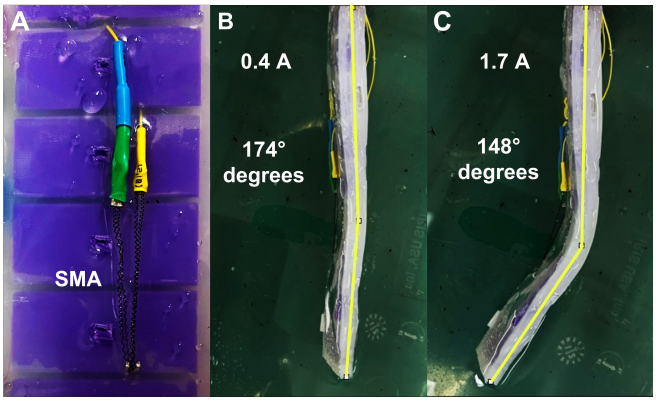


Fig. 3. **Characterization of flagella with embedded SMA.** (A) Close front view of SMA embedded flagella. (B-C) Bending angles of the flagella when SMA is under 0.4 and 1.7 A loads, respectively. Side view.

actuator within the flagellum is activated, inducing asymmetric bending, and (ii) the DC motor speed is reduced. The combination of morphological asymmetry and reduced propulsion velocity increases turning sharpness, resulting in a smaller turning radius and enabling controlled steering toward the light source.

b) Flagellum: It is fabricated from Ecoflex 00-30, a soft silicone material, with a rectangular cross-section (width = 40 mm, thickness = 5 mm; Fig. 2). Effective forward propulsion requires the flagellum to maintain axial alignment with the robot body while allowing wave-like deformation. Initially, we tested a fully soft flagellum configuration; SMA actuation caused buckling, asymmetry, and out-of-plane deformation, which reduced directional consistency in testing. To address this, rigid PLA "bones" are embedded within the silicone structure, forming a soft–rigid hybrid flagellum. The Ecoflex silicone preserves flexible oscillatory motion, while the rigid supports improve structural stability, reduce uncontrolled deformation, and enhance trajectory consistency (Fig. 1B, 2A).

Directional manipulation is achieved using a NiTi SMA spring, with a free length of 60 mm and a diameter of 1 mm. The spring is positioned near the flagellum and mechanically coupled to it to induce asymmetric bending upon contraction. Electrical lead wires connect the SMA spring to the actuation circuit and do not contribute mechanically to the deformation.

C. Flagellar Characterization

To investigate the curvature profiles generated by the Shape Memory Alloy (SMA) actuator, and to find the appropriate heating current, static characterization experiments were conducted in a viscous medium (vegetable glycerin, Fig. 3). Constant DC currents were applied to facilitate thermal activation and phase transformation within the SMA. The resulting steady-state bending angles were quantified to establish the relationship between input current and the actuator's resultant deformation.

At a low-level input of $0.2\,\mathrm{A}$, the actuator maintained a baseline interior angle of $177°$. Incrementing the current to $1\,\mathrm{A}$ intensified the thermal activation, reducing the angle to $156°$ as a result of longitudinal contraction. Further increases to $1.7\,\mathrm{A}$ yielded angle of $148°$. At $2.2\,\mathrm{A}$, the displacement was measured approximately $149°$, demonstrating an asymptotic trend of SMA phase-transformation under glycerine. Based on these characterization results, $1.7\,\mathrm{A}$ was designated as the nominal operating current for all subsequent locomotive experiments. This value was selected to maximize the curvature profile while maintaining a robust safety margin below the threshold of electrical instability. Experimental observations indicated that currents exceeding $2.4\,\mathrm{A}$ induced localized electrical arcing, posing a significant risk of dielectric breakdown or irreversible thermal degradation of the actuator assembly. Consequently, the selection of $1.7\,\mathrm{A}$ represents an optimized compromise between mechanical power output and long-term electrical reliability.

D. Experimental Setup and Procedure

Experimental characterization was conducted within a specialized glass tank ($123 \times 41 \times 47$ cm) filled with reagent-grade vegetable glycerin. At a controlled temperature of 20°C, the medium exhibits a dynamic viscosity of 1.49 Pa·s and a density of 1070 kg/m³ (Fig. 4). This high-viscosity environment is critical for dynamic scaling; by increasing the fluid resistance, we ensure the robotic platform operates within a low Reynolds number regime (SI Movie 00:15-00:20). This effectively emulates the overdamped fluidic constraints faced by microscopic organisms, where viscous forces dominate over inertial effects, allowing for a direct comparison between the macro-scale robot and its biological counterparts.

To capture the three-dimensional kinematics of the swimmer, we employed a dual-view optical tracking system consisting of two high-definition Logitech webcams positioned at the top and side of the tank. The experimental volume was illuminated using high-intensity LED strips, which provided a uniform light field to enhance image contrast and ensure high-fidelity tracking of the flagellar waveforms against the viscous background.

For each experimental condition, three independent trials were conducted. At the beginning of each trial, the robot was positioned at the center of the tank, sufficiently far from the boundaries to minimize wall effects. The initial body orientation was aligned with the tank reference frame to ensure consistent starting conditions. For straight-swimming and turning-rate characterization, motion was analyzed over an 8-second interval. For full-trajectory visualization experiments, data were recorded over 43 seconds to capture the complete swimming path. The fluid was allowed to settle between trials before restarting the experiment. Reported kinematic quantities are computed from the tracked trajectories and presented as mean ± standard deviation across the three trials.

III. Low Reynolds Number Hydrodynamics

In the microscopic realm, the fluid dynamics are characterized by a Reynolds number ($Re = \rho U L/\mu$) that is

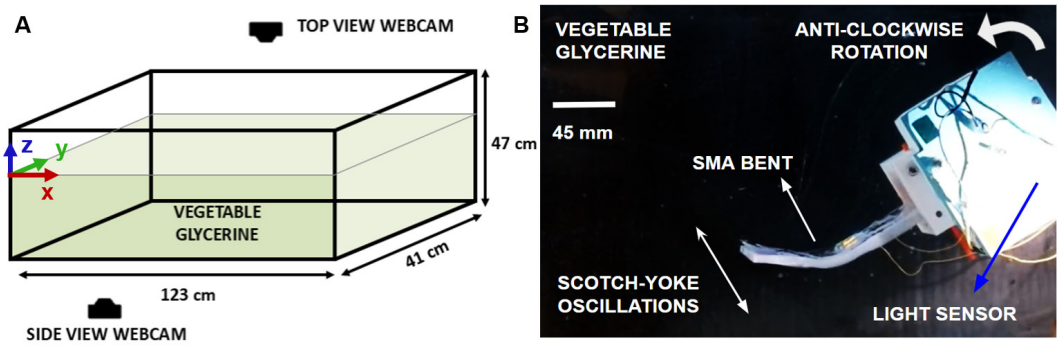


Fig. 4. **Experimental setup. A.** Schematic of the experimental setup ($123 \times 41 \times 47$ cm) filled with high-viscosity vegetable glycerin to achieve a low Reynolds number ($Re \ll 1$) regime **(B)** The top view shows the robot's anti-clockwise rotation dominated by the sma-bent asymmetric flagella, which is driven by oscillations of the flagellum.

typically several orders of magnitude smaller than unity. In this regime, viscous dissipation overwhelmingly dominates inertial effects [3]. Consequently, the inertial terms in the incompressible Navier–Stokes equations become negligible, simplifying the governing equations to the linear, time-independent Stokes form:

$$\mu \nabla^2 \mathbf{u} = \nabla p, \quad \nabla \cdot \mathbf{u} = 0 \tag{1}$$

These equations imply that the flow field is governed by the swimmer's instantaneous shape and motion, making flagellar morphology a direct determinant of the resulting hydrodynamic forces and torques. For net propulsion, these morphological changes must form a non-reciprocal (i.e., non-time-reversible) cycle, such that the forward and reverse strokes do not retrace the same sequence of shapes, as would occur with a rigid flagellum undergoing simple back-and-forth oscillation (SI Movie 00:16-00:19).

For slender flagellated swimmers, the fluid–structure interaction is modeled via Resistive Force Theory (RFT). This local approximation relates the viscous force per unit length, $\mathbf{f}(s)$, to the local filament velocity, $\mathbf{v}(s)$, as:

$$\mathbf{f}(s) = -\left(\xi_{\parallel}\mathbf{v}_{\parallel} + \xi_{\perp}\mathbf{v}_{\perp}\right) \tag{2}$$

where $\mathbf{v}_{\parallel}$ and $\mathbf{v}_{\perp}$ represent the tangential and normal velocity components relative to the filament centerline. A critical requirement for propulsion in the Stokes regime is drag anisotropy; for sufficiently slender filaments, the ratio of coefficients is $\xi_{\perp}/\xi_{\parallel} \approx 2$ [16], [17]. This anisotropy ensures that the drag experienced during a transverse stroke differs from a longitudinal one, thereby enabling the generation of net thrust from non-reciprocal deformations. The global hydrodynamic influence on the swimmer is determined by integrating these local distributions along the flagellar length L:

$$\mathbf{F} = \int_0^L \mathbf{f}(s)\, ds \quad \text{and} \quad \mathbf{M} = \int_0^L \mathbf{r}(s) \times \mathbf{f}(s)\, ds \tag{3}$$

where $\mathbf{r}(s)$ is the position vector from the swimmer's center of mass to the point s. Exploiting the linearity and quasi-static nature of Stokes flow, the total force and torque are linearly coupled to the swimmer's instantaneous translational ($\mathbf{v}_0$) and rotational ($\boldsymbol{\omega}_0$) velocities through a configuration-dependent resistance matrix, $\mathbf{R} \in \mathbb{R}^{6\times 6}$:

$$\begin{bmatrix} \mathbf{F} \\ \mathbf{M} \end{bmatrix} = \mathbf{R} \begin{bmatrix} \mathbf{v}_0 \\ \boldsymbol{\omega}_0 \end{bmatrix} \tag{4}$$

Under the force- and torque-free constraints inherent to self-propulsion, the swimmer's velocities are uniquely determined by the balance between the propulsive hydrodynamic forces generated by the flagellum and the resistive drag of the body.

IV. Experimental Results

A. Straight Motion Analysis

Straight-line locomotion was evaluated over an 8-second interval under different propulsion levels and SMA placements (Fig.5- top, Table I). At 255 PWM with proximal SMA placement, the robot achieved an average forward speed of 6.92 ± 0.70 mm/s, demonstrating consistent forward progression. At 150 PWM, the average speed decreased to 3.85 ± 0.35 mm/s, indicating reduced propulsion while maintaining repeatability across trials. At 255 PWM with the SMA positioned toward the mid/distal region of the flagellum, the robot reached the highest average speed of 7.96 ± 0.10 mm/s, exhibiting both increased propulsion and strong trial-to-trial consistency. Notably, when the SMA was attached closer to the mid/distal tip, straight-line motion was observed to be more stable, with reduced lateral deviation and improved trajectory consistency compared to proximal placement.

To better understand the propulsion mechanism during straight swimming, we analyzed the instantaneous curvature distribution of the flagellum using representative phase

TABLE I
Forward Performance of the Robot

Condition	Forward Speed (mm/s)
150 PWM (Prox)	3.85 ± 0.35
255 PWM (Prox)	6.92 ± 0.70
255 PWM (Mid/Dist)	7.96 ± 0.10

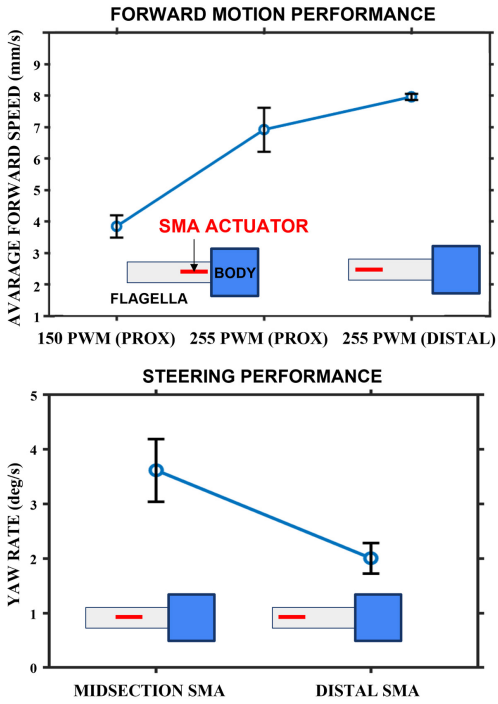


Fig. 5. **Experimental Results.** (Top) Average forward velocity with different motor frequencies (150 and 255 PWM) and SMA orientation on the flagella. (Bottom) Steering performance of the robot with two different SMA orientations (midsection and distal).

snapshots from the experiments (Fig. 6). Multiple curvature radii were measured along the filament at distinct time instants within one oscillation cycle, allowing us to capture the dominant deformation phases of the flagellum. At the beginning of the stroke, the proximal portion of the filament exhibits moderate bending with local curvature radii on the order of $57\,\mathrm{mm}$, while the distal region remains relatively extended with radii approaching $90\,\mathrm{mm}$. As the oscillation progresses, the curvature distribution shifts along the filament and bends in the opposite direction, with subsequent phases showing reduced radii in different segments of the filament, approximately 40–$47\,\mathrm{mm}$. The corresponding space–time curvature plot shows a balanced distribution of positive and negative curvature regions as the localized bending propagates along the flagellum in a repeatable oscillatory pattern during forward propulsion.

Physically, this stable forward propulsion of the hybrid flagellum is governed by the drag anisotropy described in Section III. In accordance with Resistive Force Theory (Eq. 2), the normal drag coefficient is approximately twice the tangential drag coefficient ($\xi_\perp/\xi_\parallel \approx 2$). This anisotropy allows the transverse, non-reciprocal bending waves propagating down the flagellum (as captured in the phase snapshots in Fig. 6) to generate a net forward thrust (F) that overcomes the viscous drag of the robot's body.

B. Steering Analysis

Steering was achieved by using light as an external switch to transition between locomotion modes (Fig.4B). When the light intensity exceeded a predefined threshold, the embedded SMA actuator was activated, producing controlled curvature along the flagellum and changing the swimmer's trajectory. In this implementation, light was used as a wireless trigger for switching from straight swimming to turning. Simultaneously with the SMA actuation, the propulsion motor speed was reduced. This combination of actuator-induced asymmetry and decreased forward velocity increased the path curvature, enabling sharper turns. When light intensity remained below the threshold, the SMA remained inactive (soft) and the motor operated at nominal speed, resulting in straight locomotion. Thus, steering behavior emerged from a binary morphological change coupled with propulsion modulation.

Turning performance was quantified using mean yaw rate (°/s). Our results indicate that actuator placement is a primary determinant of steering efficacy (Fig. 5- bottom). When SMA was integrated into the midsection of the flagellum, the system exhibited a pronounced turning response, characterized by a mean yaw rate of $3.62 \pm 0.58°/\mathrm{s}$ and a high-curvature trajectory with a radius of 3.95 ± 2.90 mm. In the distal configuration, the steering authority diminished, yielding a reduced yaw rate of $2.01 \pm 0.28°/\mathrm{s}$ and a significantly larger trajectory radius of 124.17 ± 35.07 mm.

Conversely, proximal placement (near the base) resulted in the weakest turning effect. This configuration also compromised longitudinal stability, leading to a degradation in the distinction between directed propulsion and turning maneuvers. The findings suggest that the midsection of the flexible appendage serves as the optimal site for elastohydrodynamic symmetry breaking, providing the greatest degree of steering authority and the most well-defined transitions between motion states.

Similar to the straight-swimming analysis, multiple curvature radii were measured along the filament during representative phases of the actuation cycle. The snapshots show that SMA-induced bending shifts the flagellar waveform toward one side of the swimmer, with local curvature radii ranging from approximately 36 mm to 60 mm. This asymmetric deformation is also evident in the space–time curvature plots, where the steering case exhibits weaker curvature in one direction compared with the forward-motion case, indicating a directionally biased bending pattern during turning (Fig. 6).

C. Steering emerges from SMA-induced Hydrodynamic Force Redistribution

When the SMA actuator is activated, the curvature distribution along the flagellum changes significantly, producing a persistent geometric bias that modifies the oscillatory waveform (Fig. 6). This geometric bias changes the local orientation and projected shape of the flagellum during oscillation, thereby altering the distribution of viscous drag forces along the filament. Although the fluid properties and intrinsic drag coefficients remain unchanged, the SMA-induced curvature creates an asymmetric hydrodynamic force profile, which generates a lateral force imbalance and a net yaw torque on the swimmer. Thus, the shape-dependent drag

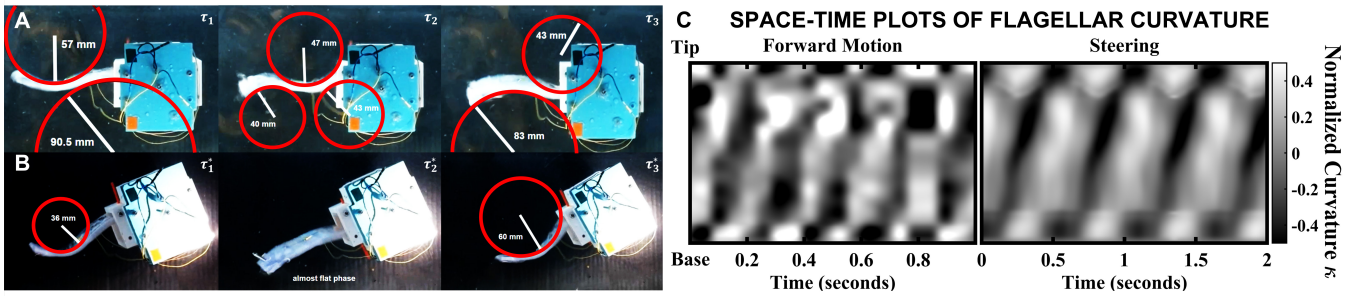


Fig. 6. **Straight locomotion and steering experiment snapshots with flagellar buckling radii and curvature evolution.** (A) Straight-locomotion sequence showing three distinct flagellar shapes, τ_1, τ_2, and τ_3, within one motor-rotation cycle during forward propulsion. (B) Steering sequence showing three distinct flagellar shapes, τ_1^*, τ_2^*, and τ_3^*, within one motor-rotation cycle after SMA activation, where asymmetric flagellar buckling produces directional turning. (C) Space–time plots of normalized flagellar curvature, $\kappa_{\text{norm}} = \kappa / \max|\kappa|$.

force redistribution is the primary physical pathway by which SMA-induced symmetry breaking produces steering.

A possible secondary contribution to the observed steering is the lateral redistribution of mass caused by SMA contraction. However, this effect is expected to be negligible in the present design compared with the curvature-induced hydrodynamic force asymmetry discussed above. The dominant mass of the swimmer is concentrated in the rigid body, electronics housing, battery, and stabilizing weight box, whereas SMA activation produces only a small lateral displacement within the comparatively lightweight flagellar structure. In our previous study [14], lateral mass imbalance was intentionally introduced at a substantially larger scale and was shown to produce observable changes in the resting posture and turning behavior of the swimmer and its flagellum. Such posture changes were not observed in the present experiments. Therefore, although minor center-of-mass effects cannot be completely excluded, the observed steering is expected to be governed primarily by SMA-induced hydrodynamic force redistribution rather than by mass redistribution.

D. Switching From Straight Motion to Steering

To evaluate the transition from straight locomotion to steering, we conducted light-triggered switching experiments (Fig. 8). The robot was initially driven under the straight-swimming condition to establish a stable forward trajectory. At $t = 8$ s, a directional light stimulus was introduced, triggering the steering mode (SI Movie 00:43-00:58). Prior to illumination, all trials displayed straight directional stability, with heading angles (θ) characterized only by minor oscillations consistent with the flapping frequency of the robot's body. Robot body oscillations arise from the instantaneous force- and torque-free conditions at low Reynolds number, whereby the hydrodynamic forces and torques generated by the oscillating flagellum are balanced by compensatory motion of the body.

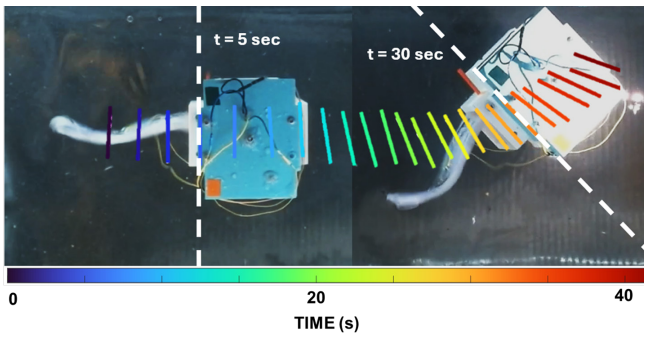


Fig. 7. **Snapshots from the straight motion to turning experiments.** Evolution of the robot's back edge over time. The trajectory begins with 8 seconds of straight motion. Upon light stimulation, the robot initiates steering, resulting in a gradual change in orientation.

When the SMA is activated, the resulting structural asymmetry shifts the flagellum's neutral axis, breaking the lateral symmetry of the stroke. In the context of the force- and torque-free constraints of self-propulsion (Eq. 4), this geometric bias alters the configuration-dependent resistance matrix R. The asymmetric stroke generates a non-zero net hydrodynamic torque (M), which drives the rotational velocity (ω_0) of the swimmer. This is experimentally reflected in the sustained yaw rates reported in Table II.

TABLE II
TURNING PERFORMANCE OF THE ROBOT

SMA Placement	Yaw Rate (deg/s)	Turning Radius (mm)
Midsection SMA	3.62 ± 0.58	3.95 ± 2.90
Distal SMA	2.01 ± 0.28	124.17 ± 35.07

After light detection, the system exhibited an approximately 2 s total response delay, consisting of an approximately 1 s electrical/control delay before SMA current onset and an approximately 1 s thermomechanical latency associated with heating and the SMA phase transition. This response delay may limit high-speed autonomous navigation, where rapid heading correction or obstacle avoidance is required. However, because locomotion in the present low-Reynolds-number environment is slow and overdamped, the delay remains compatible with gradual steering at the tested speeds. Future designs could reduce this latency through optimized SMA geometry, improved thermal management, or predictive control strategies.

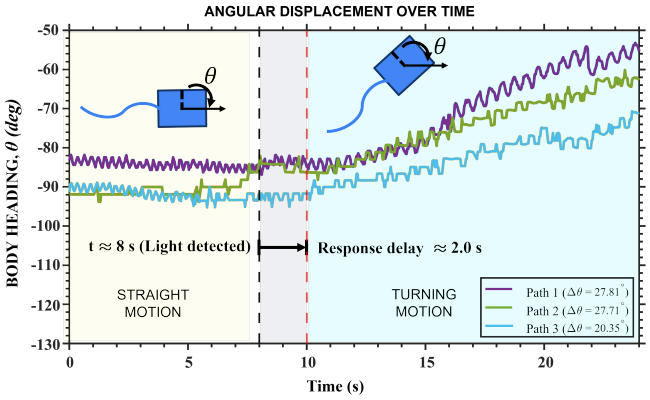


Fig. 8. **Angular displacement of the robot over time with respect to the initial robot frame.** The oscillations arise from low Reynolds number swimming dynamics, where periodic flagellar actuation induces corresponding body oscillations due to instantaneous force and torque balance.

Following the delay, the heading angle began to diverge consistently across trials. Quantitatively, Path 1 demonstrated the largest heading deviation, with an angular displacement of $\Delta\theta \approx 27.8°$, while Path 2 and Path 3 exhibited deviations of $\approx$ $27.7°$ and $\approx$ $20.4°$, respectively. All trajectories showed heading divergence after light-triggered activation, demonstrating that the integration of on-board sensing, thermal actuation, and soft-body elasticity provides a reliable mechanism for mode switching in viscous environments. The results are summarized in Table II.

V. Conclusion and Future Work

We have presented a soft/rigid (hybrid) flagellated robotic platform capable of transitioning between stable straight propulsion and controlled steering in a low Reynolds number ($Re \ll 1$) environment. By leveraging a light-triggered SMA integrated into a flexible filament, we demonstrated how localized thermal activation can break the structural symmetry of the flagellum, thereby modulating the net hydrodynamic wrench. Our experimental characterization establishes that the spatial positioning of the actuator along the flagellum is a critical determinant of steering authority; specifically, mid-section placement optimizes the trade-off between propulsive efficiency and rotational yaw rate.

This work demonstrates that a compact SMA actuator can reconfigure a continuously motor-driven soft flagellum, enabling transitions between straight swimming and turning through a simple on–off steering input. The flagellum converts this low-complexity, approximately binary actuation into directional control without distributed actuators or complex steering hardware.

Future work will investigate the proposed steering mechanism across a broader range of Reynolds-number regimes by varying fluid viscosity to demonstrate the generality and potential applicability of the proposed approach. Additionally, we aim to develop predictive fluid–structure interaction models and control strategies that capture the nonlinear coupling between large flagellar deformation and the surrounding flow, ultimately enabling autonomous navigation through morphological control.

Acknowledgment

E.P. Aydin designed the robot and experimental setup and conducted the experiments and analysis. Y. Ozkan-Aydin supervised the research and provided project administration. Both authors contributed to the writing and revision of the manuscript, and approved the final manuscript. The authors would like to thank the members of MiNiRoLab @ ND for their support and valuable feedback.

References

[1] M. Sitti, H. Ceylan, W. Hu, J. Giltinan, M. Turan, S. Yim, and E. Diller, "Biomedical Applications of Untethered Mobile Milli/Microrobots," *Proceedings of the IEEE*, vol. 103, no. 2, pp. 205–224, Feb. 2015.

[2] S. Palagi and P. Fischer, "Bioinspired microrobots," *Nature Reviews Materials*, vol. 3, no. 6, pp. 113–124, Jun. 2018.

[3] E. M. Purcell, "Life at low Reynolds number," *American Journal of Physics*, vol. 45, no. 1, pp. 3–11, Jan. 1977.

[4] H. C. Berg and R. A. Anderson, "Bacteria swim by rotating their flagellar filaments," *Nature*, vol. 245, no. 5425, pp. 380–382, 1973.

[5] J. Elgeti, R. G. Winkler, and G. Gompper, "Physics of microswimmers—single particle motion and collective behavior: a review," *Reports on Progress in Physics*, vol. 78, no. 5, p. 056601, Apr. 2015.

[6] K. Son, J. Guasto, and R. Stocker, "Bacteria can exploit a flagellar buckling instability to change direction," *Nature Physics*, vol. 9, pp. 494–498, 07 2013.

[7] B. J. Walker, C. Moreau, T. L. Robinson, Z. J. Xu, D. I. Goldman, E. A. Gaffney, and K. Y. Wan, "Tunable asymmetric swimming in biflagellate microswimmers," 2026. [Online]. Available: https://arxiv.org/abs/2602.17521

[8] A. Nazaripouya, N. C. Chikere, and Y. Ozkan-Aydin, "Embodied intelligence through appendages in biology and robotics," *IOP Conference Series: Materials Science and Engineering*, vol. 1343, no. 1, p. 012009, mar 2026. [Online]. Available: https://doi.org/10.1088/1757-899X/1343/1/012009

[9] N. Chikere and Y. Ozkan-Aydin, "Harnessing Flagella Dynamics for Enhanced Robot Locomotion at Low Reynolds Number," *IEEE Robotics and Automation Letters*, vol. 9, no. 5, pp. 4138–4145, May 2024.

[10] N. C. Chikere, S. L. Voticky, Q. D. Tran, and Y. Ozkan-Aydin, "Flagellar Swimming at Low Reynolds Numbers: Zoospore-Inspired Robotic Swimmers with Dual Flagella for High-Speed Locomotion," Dec. 2024.

[11] F. Z. Temel, A. G. Erman, and S. Yesilyurt, "Characterization and Modeling of Biomimetic Untethered Robots Swimming in Viscous Fluids Inside Circular Channels," *IEEE/ASME Transactions on Mechatronics*, vol. 19, no. 5, pp. 1562–1573, Oct. 2014.

[12] C. H. Wiggins and R. E. Goldstein, "Flexive and propulsive dynamics of elastica at low reynolds number," *Phys. Rev. Lett.*, vol. 80, pp. 3879–3882, Apr 1998. [Online]. Available: https://link.aps.org/doi/10.1103/PhysRevLett.80.3879

[13] T. S. Yu, E. Lauga, and A. E. Hosoi, "Experimental investigations of elastic tail propulsion at low reynolds number," *Physics of Fluids*, vol. 18, no. 9, 2006. [Online]. Available: http://dx.doi.org/10.1063/1.2349585

[14] E. P. Aydin, N. C. Chikere, V. Attupuram, and Y. Ozkan-Aydin, "Swimming dynamics of a soft flagellated robot in low reynolds number environment," in *International Symposium on Experimental Robotics (ISER)*, 2025, to appear in Experimental Robotics, Springer Proceedings in Advanced Robotics.

[15] I. R. Gibbons, "Cilia and flagella of eukaryotes," *The Journal of Cell Biology*, vol. 91, no. 3 Pt 2, pp. 107s–124s, Dec. 1981.

[16] J. Gray and G. J. Hancock, "The propulsion of sea-urchin spermatozoa," *Journal of Experimental Biology*, vol. 32, no. 4, pp. 802–814, 12 1955.

[17] E. Lauga and T. R. Powers, "The hydrodynamics of swimming microorganisms," *Reports on Progress in Physics*, vol. 72, no. 9, 2009.